Hindawi Publishing Corporation
International Journal of Optics
Volume 2012, Article ID 517591, 18 pages
doi:10.1155/2012/517591

Review Article

Interferometry with Vortices

P. Senthilkumaran,[1] Jan Masajada,[2] and Shunichi Sato[3]

[1] *Department of Physics, Indian Institute of Technology-Delhi, New Delhi 110 016, India*
[2] *Institute of Physics, Wroclaw University of Technology, Wybrzeze Wyspianskiego 27, 50-370 Wroclaw, Poland*
[3] *Institute of Multidisciplinary Research for Advanced Materials, Tohoku University, Katahira 2-1-1, Aoba-ku, Sendai 980-8577, Japan*

Correspondence should be addressed to P. Senthilkumaran, psenthilk@yahoo.com

Received 15 April 2011; Revised 24 June 2011; Accepted 4 July 2011

Academic Editor: Takashige Omatsu

Interference of optical beams with optical vortices is often encountered in singular optics. Since interferometry makes the phase observable by intensity measurement, it brings out a host of applications and helps to understand the optical vortex. In this article we present an optical vortex interferometer that can be used in optical testing and has the potential to increase the accuracy of measurements. In an optical vortex interferometer (OVI), a lattice of vortices is formed, and the movement of the cores of these vortices is tracked when one of the interfering beams is deformed. Instead of multiple vortices in an OVI, an isolated single vortex also finds applications in optical testing. Finally, singularity in scalar and vector fields is presented, and the relation between them is illustrated by the superposition of these beams.

1. Introduction

Phase singularities in light waves appear at points or lines in a beam cross section, where the phase of the wave changes abruptly [1–6]. When this abrupt phase change occurs along a line, it is called edge dislocation, and when it occurs at a point, it is called a screw dislocation. Screw dislocation type phase singularity is also called an optical vortex. The singular point with undefined phase and zero amplitude forms the vortex core. A wavefront with optical vortex (OV) has a characteristic helical geometry. As the vortex beam propagates, this zero amplitude point draws a curve in space. The helical wavefront winds about this dark thread of amplitude. The helix may be left- or right-handed, and accordingly the vortex is considered to possess positive or negative topological charge. Optical vortices possess a number of interesting features. On the flip side, they can cause stagnation problems in phase retrieval where wavefront geometry is reconstructed [7, 8] and in diffractive optics [9, 10]. On the positive side, since the seminal work published by Nye and Berry [1], hundreds of papers have been published on various aspects of the OVs. Large number of papers is devoted to optical vortex applications. In a vortex coronagraph an optical vortex lens is used as a filter that enables detection of a feeble star in bright background [11–13]. Optical vortices are useful in optical tweezers with dark traps [14–17]. They are useful in fluorescence microscopy where the STED (stimulated emission depletion) pulse is used for dumping the fluorescence response of the molecule located outside the dark core of the optical vortex [18–20]. Vortices are useful in collimation testing and in the detection of elevation and depression of surfaces from a single interferogram. Further vortex interferograms can be used as signatures of vortices in the detection process. Optical recording of these interferograms can also be used as holograms for the generation of OVs. Vortices can be used to generate inhomogeneously polarized beams. OVs carry non-zero orbital angular momentum (OAM) in addition to the momentum related to polarization [21, 22]. The OAM arises due to the spiraling of Poynting vector in the singular beam. This makes optical vortices stable features of the wavefront.

In this paper we present the use of OVs in interferometry. In part I, we present optical vortex interferometer (OVI), which refers to interferometric system in which OV lattice plays a crucial role in the measurement process. In part II, we present the use of isolated single vortex in optical metrology. In the last section of part II, we discuss the role of

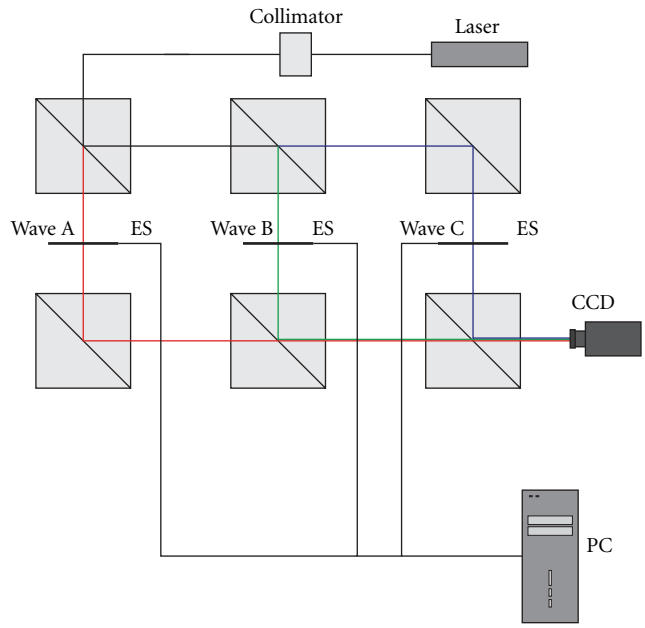

Figure 1: Six cubic beam splitters generate a set of three plane waves: A, B, C. These beams interfere and generate regular lattice of optical vortices. ESs are electronic shutters, which enable to capture the following interferograms: $A + B$, $A + C$, $B + C$, $A + B + C$. The electronic shutters are not necessary when using one-frame ($A + B + C$) measurement procedure.

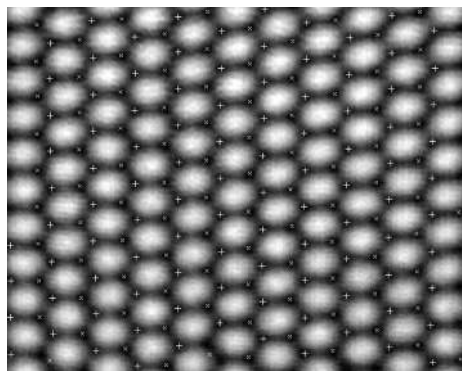

Figure 2: The Intensity distribution of the interference field obtained by three-plane waves (experiment). The position of vortex points is marked by plus signs or crosses to distinguish between two different topological charges.

vortex interferometry in the realization of inhomogeneously polarized beams.

2. Part I

2.1. Optical Vortex Lattice Interferometer. When two beams interfere in space, bright and dark surfaces due to interference are formed in the volume of overlap. When viewed at an observation plane, these surfaces appear as interference fringes in a conventional interferometer. When one of the interfering beams is modified, the fringe pattern undergoes a change, and this is tracked in conventional optical testing. But when three or more waves interfere, light vanishes at lines rather than on surfaces. In 2D, these lines appear as dark points instead of fringes. The central part of each such dark point is a vortex point, that is, an isolated point where phase is undetermined. The OVI focuses on the distribution and dynamics of these dark points.

The regular lattice of optical vortices generated by wave interference was a subject of interest prior to the work on OVI. The first papers focused on physical questions concerning the properties of electromagnetic field or more specifically the phase singularity itself [23–25]. In a multiple-beam interference, it is possible to shape and tailor the geometry of these dark threads of light in the form of loops, links and knots [26–28]. The relations between vortex lattices and polarization singularities have also been described [29]. The papers concerning general questions in the theory of electromagnetic fields have also been published in the last decade [30, 31]. The three- or more plane waves interference can also be used for photonics crystal manufacturing [32, 33].

Here we want to focus our attention on metrological aspects of vortex lattice in interference fields [34–49]. Our first goal is to show specific basic properties of the vortex lattice formed by the interference of three-plane waves [34, 35]. Figure 1 shows the basic optical setup for three-plane-wave OVI, and Figure 2 shows an interference pattern obtained in such an interferometer.

The resultant field, due to the interference, consists of vortices arranged in a regular fashion. The net charge in the pattern is zero, which means that there is an equal number of positive and negative charges in the lattice. The vortex lattice can be decomposed into two sublattices each consisting of vortex points having the same topological charge (Figure 2). It is useful to use phasors and constant angle lines (CALs) [37, 38] to have better understanding on vortex lattice creation and properties. The CALs of two

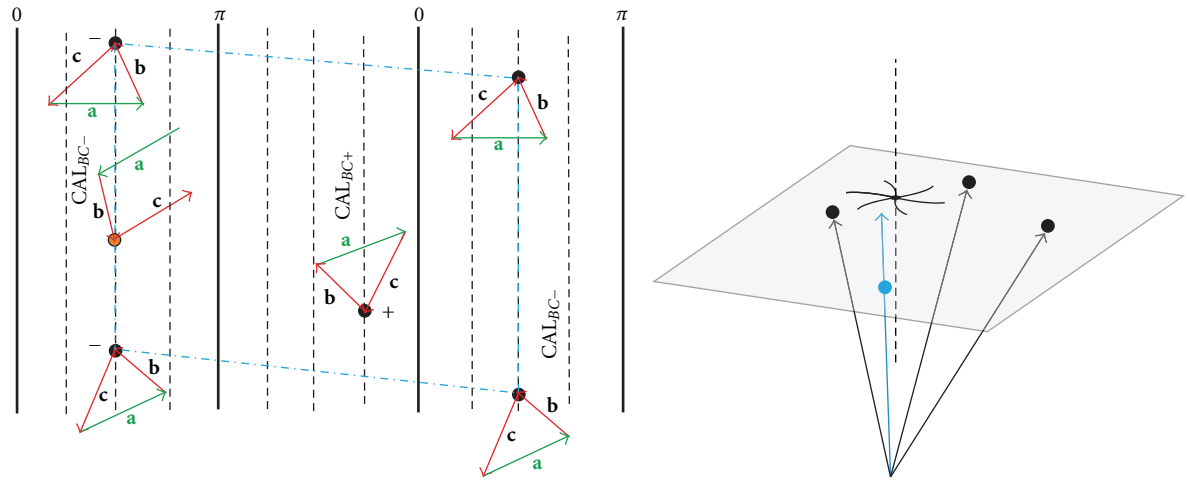

FIGURE 3: (a) A set of CALs (dashed lines) of two interfering waves B and C. By adding the third wave—wave A—a regular vortex lattice is generated. The arrows **a**, **b**, and **c** are phasors of wave A, B, and C, respectively. The OVs appear at points where the three phasors form a triangle. The whole pattern can be divided into two subsequently appearing regions: the region with positive vortices and the region with negative vortices, respectively. The CALs$_{BC}$ representing angle value 0 and π (bold lines) are borders between these two regions. Vortex points are marked by black dots. The four neighboring vortices of the same topological charge form an equilateral basic cell (dash dotted blue line). (b) The ends of three non-collinear wave vectors define the OVI plane. The optical vortex generated by the three-plane waves moves along the straight line (dashed line) perpendicular to the OVI plane. When adding one more wavevector (blue in this Figure) the OVI plane cannot be defined, but in very specific cases.

waves B and C (CALs$_{BC}$) is a line of constant phase angle between these two waves. The CALs are defined at the plane at which interference pattern is observed. Figure 3 explains why the regular vortex lattice is created when three-plane waves interfere [34, 35, 37–39].

The vortex lattice shown in Figure 2 has a number of interesting properties, which result from two facts [38]. First, the ends of three non collinear wave vectors determine a plane uniquely (OVI plane (Figure 3(b)), and, second, the relative phases between interfering waves are defined by their amplitudes (at vortex points). It can be concluded from the above that (a) the vortex lattice moves as a rigid body, when the phase of one or more of three waves is changed, (b) changing the amplitude of the interfering waves has no influence on the vortex positive (negative) sublattice geometry; however, both sublattices change their relative positions, (c) in space optical vortices travel along lines perpendicular to the OVI plane (Figure 3(b)), and (d) it is easy to determine formulas for vortex points positions [38] as follows:

$$\begin{aligned} x_P &= \frac{(-\delta_{AB} + \pi - \gamma_{AB} + 2\pi l)k'_{yC}}{k'_{xB}k'_{yC} - k'_{xC}k'_{yB}} \\ &\quad + \frac{(\delta_{CA} - \pi - \gamma_{AC} - 2\pi m)k'_{yB}}{k'_{xB}k'_{yC} - k'_{xC}k'_{yB}}, \\ x_N &= \frac{(-\delta_{AB} + \pi + \gamma_{AC} + 2\pi l)k'_{yC}}{k'_{xB}k'_{yC} - k'_{xC}k'_{yB}} \\ &\quad + \frac{(\delta_{CA} - \pi + \gamma_{AC} - 2\pi m)k'_{yB}}{k'_{xB}k'_{yC} - k'_{xC}k'_{yB}}. \end{aligned} \tag{1}$$

In the above formulas, index N and P indicate negative and positive sublattices, respectively. δ_{QR} is a relative phase difference between waves Q and R at the origin of the reference frame, γ_{qr} is a triangle angle between phasor q and r; $q, r \in [a, b, c]$ (see Figure 3), $k_{\mu Q}$ is the μ-coordinate of the wavevector of wave $Q, \mu \in [x, y, z]$, $Q, R \in [A, B, C]$, and

$$\begin{aligned} k'_{xQ} &= k_{xQ} - k_{xA}, \\ k'_{yQ} &= k_{yQ} - k_{yA}. \end{aligned} \tag{2}$$

The y-coordinates may be expressed by x-coordinates as follows:

$$\begin{aligned} y_P &= \frac{-k'_{xB}}{k'_{yB}}x_P + \frac{\delta_A - \delta_B + \pi - \gamma_{ab} + 2\pi l}{k'_{yB}}, \\ y_N &= \frac{-k'_{xC}}{k'_{yC}}x_N + \frac{\delta_A - \delta_C + \pi + \gamma_{ac} + 2\pi m}{k'_{yB}}. \end{aligned} \tag{3}$$

When placing subsequent integer numbers m and l into formulas (1) and (3), the position of the same vortex point may be obtained many times, especially for highly symmetrical arrangement of interfering waves. Special reduction procedures must be applied to avoid such a multiplication. Vortex points move along straight lines perpendicular to the OVI plane. The direction of this path can be determined by formulas [37, 38]

$$\begin{aligned} \Delta x &= \frac{k'_{zC}k'_{yB} - k'_{yC}k'_{zB}}{k'_{xB}k'_{yC} - k'_{xC}k'_{yB}}\Delta z, \\ \Delta y &= \frac{k'_{zB}k'_{xC} - k'_{xB}k'_{zC}}{k'_{xB}k'_{yC} - k'_{xC}k'_{yB}}\Delta z. \end{aligned} \tag{4}$$

Adding more than three-plane waves results in a less regular vortex lattice, and the special properties described above are no longer valid [38]. More precisely, the regular vortex lattice can still be generated but only in case of very specific wavevector configurations (for example, when the ends of wavevectors touch the same plane).

After presenting the specific basic properties of the vortex lattice formed by the interference of three-plane waves, let us present how OVI is useful in optical testing. The sample under measurement is introduced in one or more beams of the OVI. This in turn disturbs the vortex lattice geometry. These changes can be related to the value of the physical quantity being measured. The most basic example is wave tilt measurement [39–43]. The direction of propagation of the wave A, for example, can be changed by inserting an optical wedge. Figure 4 shows the response of the vortex lattice due to wedge insertion in wave A [42].

Using the properties listed above, we can derive formulas for the wave tilt through x and y axes separately. Only one measurement step is necessary for that. Instead of calculating these two angles, we can calculate the wedge angle and its orientation.

Two methods have been proposed to analyze vortex lattice dynamics. The first method is based on the analysis of vortex triplet geometry. Vortex triplet consists of three vortex points which do not lie along a single line [37, 40–42]. Having 300–400 vortex points, we can find about one million vortex triplets. The second method uses elementary cells [42] as shown in Figure 5.

Both methods are compared, and proper formulas for computing wave tilt are derived in [42]. The interesting point is that OVI enables a sound statistical analysis of the measurement, which usually is not possible in interferometric measurements. Figure 6 shows these results.

Promising versions of the OVI are compact setups using one [44, 45] or two Wollaston prisms (one-way OVI) [46]. They support a limited access to the interfering waves but are smaller and more stable. Simple and compact one-way OVI is equivalent to a four-wave OVI. As was mentioned above, the four-wave system generates less regular vortex lattice. However, this two Wollaston prism setup generates waves at very symmetrical distribution. As a result, the vortex lattice is more regular. The one-way OVI can be used for tracing the dynamic changes of light polarization or briefirngent sample properties [47, 48]. In a single measurement, both azimuth angle and ellipticity or ellipticity and phase difference between fast and slow axes of the birefringent medium can be determined. Figure 7 shows exemplary results of such a measurement.

A more sophisticated setup is shown in Figure 8. One version of these systems generates a rectangular table of all polarization states of light [36]. Along the horizontal line, the polarization states of subsequent points differ in their azimuth while going along the vertical line they differ in their ellipticity. Using the system in the reverse way, the optical vortex is generated in the observation plane. The coordinates of this vortex point identify the polarization state of the incoming light (i.e., azimuth angle and ellipticity). Joining the two one-way setups, a compact spatial polarimeter has been proposed. In a single measurement, this instrument allows the measurement of azimuth and ellipticity of the fast and slow beams and also the retardation introduced by the birefringent medium. When applying the carrier frequency method for interferogram analysis all these parameters can be determined at each pixel of the camera. This is the most ascetic polarimetric system ever proposed.

The OVI was also applied for the wavefront reconstruction [37, 39, 49]. By knowing the charge of the vortices in the vortex lattice, we can reconstruct the wavefront geometry without any ambiguities, for instance, the phase unwrapping problem, which is a characteristic of classical interferometry. There are many methods available to identify optical vortex charge for a single beam [50–53]. The methods for determining the charge sign distribution at vortex lattice are described in [54–56]. These methods can be used before measurement (as system calibration methods), and as such do not change the results of the measurements.

The accuracy and resolution of the OVI strongly depends on the accuracy of vortex point's localization. A few localization methods have been specifically designed for the OVI. The most basic is the one which searches intensity minima [57]. When supported by modern image processing techniques, this minima method can result in precise vortex localization. Moreover, more advanced methods too begin with the minima method. When compared with classical interferometry, minima method has a resolution of around $\lambda/30$. Nevertheless, we realize that by applying a more professional approach, this resolution can be improved. The big advantage of the minima method is that it works on a single interferogram. More precise methods require more than one interferogram, which means that the optical system must be stable [58]. The "triangle" method described in [57] requires four interferograms: $A + B$, $A + C$, $B + C$, and $A + B + C$, so the OVI must be equipped with fast shutters. The triangle methods result in a resolution twice as good as the minima method. An even more precise method is the phase-shifting method [59]. This method needs an extra reference wave with a phase shifter. This ensures that the vortex lattice remains undisturbed during the process. Since the topic is new, we hope that remarkable progress is still possible.

2.2. Vortex Lattices from Spherical Waves. Other ways of vortex lattice generation are also possible. We describe here the use of amplitude splitting and wavefront splitting interferometers for the same. Three pinholes on an opaque screen are illuminated by a plane wave, or a spherical wave and the diffracted waves behind the pinholes interfere to form the vortex lattice. The schematic of the experimental setup is shown in Figure 9. If the distance between the xy plane and the observation plane (x_1, y_1 plane) is large enough to treat the diffraction as Fraunhofer, the spherical waves from the three pinholes will be seen as plane waves in the observation plane which interfere to form the vortex lattice. The geometry of the lattice is decided by the relative positions of the pinholes. The positions of the vortices in the lattices

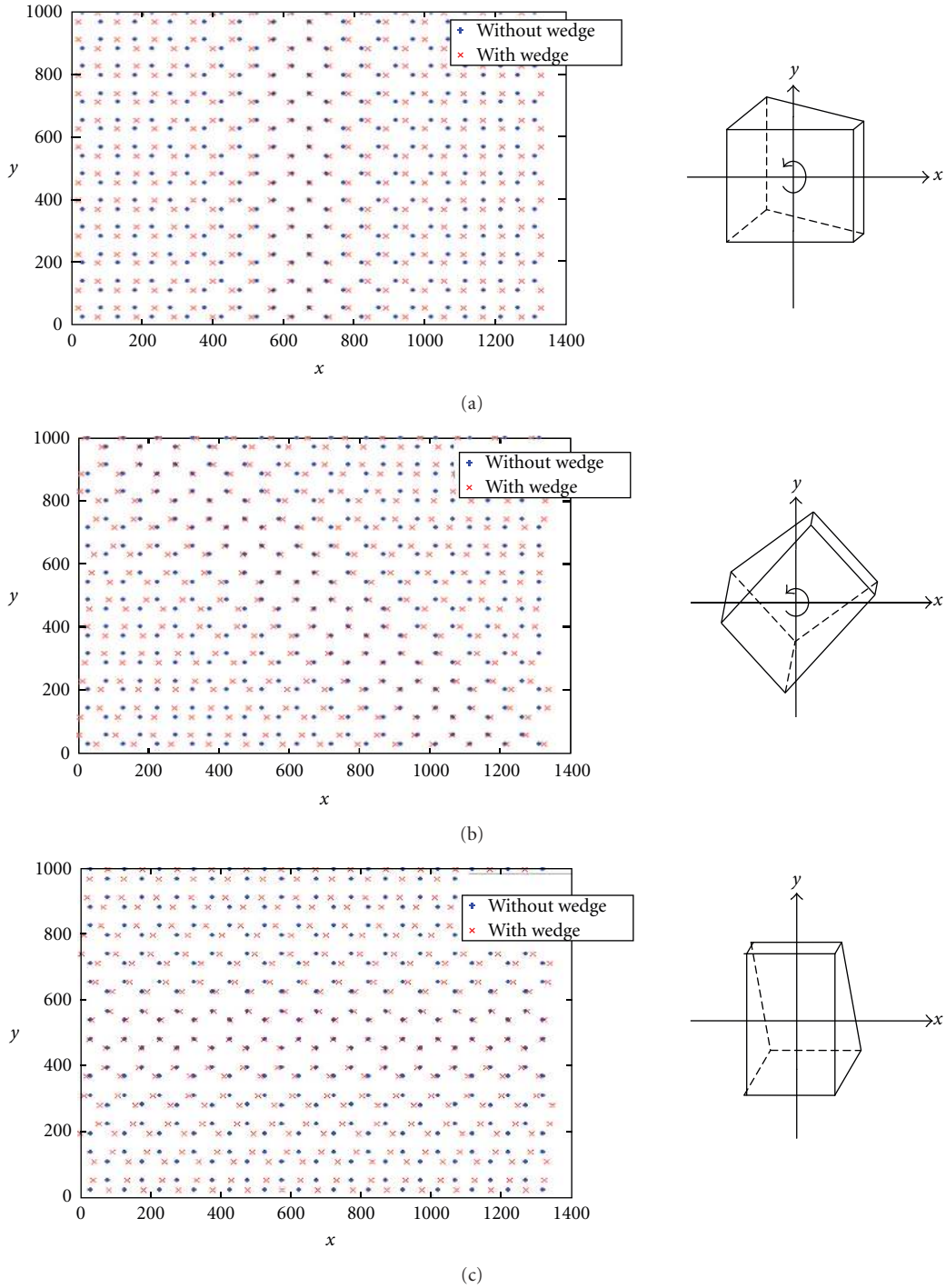

Figure 4: The position of the vortex points (expressed in pixel number) as measured without the wedge (circles) and with the wedge (crosses), (a) wedge inserted horizontally, (b) wedge inserted at $\beta = 45°$, (c) wedge inserted vertically as presented in the right corners. Deflection angle $\alpha = 20$ arcsec.

have been derived both in far- and near-field approximations and presented by Masajada et al. [60]. When the distance z between the two planes is small or when spherical waves are involved, the formation of vortex lattice still occurs and has been dealt with by Masajada et al. [60] and Ruben and Paganin [61]. Finding of analytical expression for the position of vortex points in the lattice becomes complicated when one more pinhole is added. Technically the three pinholes setup is the simplest version of OVI interferometers. The three pinholes experiment can be considered as an extension of the classical Young's double-slit experiment. We can derive formulas for the intensity minima in a simple way

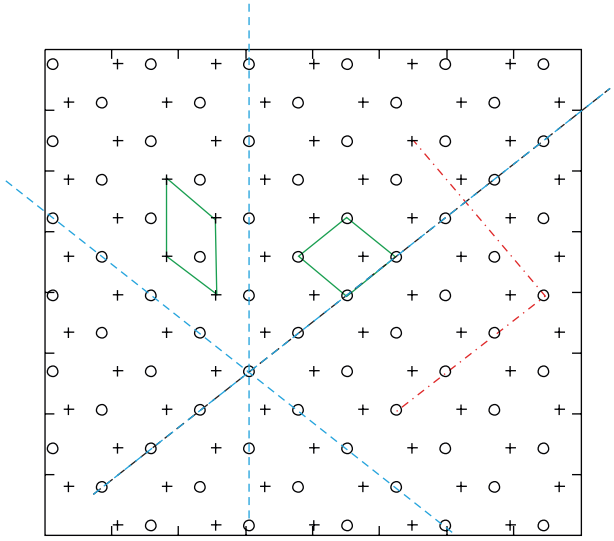

Figure 5: The vortex lattice consists of two sublattices which are marked by plus signs and circles. The CALs of wave pairs A and B, B and C, A and C are marked by dashed blue lines and are parallel to the corresponding $A+B$, $B+C$, and $A+C$ fringe systems. Figure shows an example of two cells, whose sides are determined by CALs and one triplet (red dashed-dot line). The vortex cells must be occupied by the vortex points having the same topological charge, while the triplets can be composed of any three vortex points, which are not collinear.

as in case of the later. Adding one more pinhole makes the whole problem complex.

Diffraction through the pinhole arrangement falls under the category of interference by wavefront splitting. It is also possible to generate vortex lattices by shear interferometers in which amplitude splitting of spherical waves is employed [62, 63]. In a lateral shear interferometer, interference is obtained between a test wavefront and its displaced replica. The most common configuration of lateral shear interferometer uses a plane parallel plate also called shear plate. When a test wavefront is incident on the plane parallel plate at an oblique angle, the beams reflected from the front and back surfaces of the plate are laterally displaced (sheared). The sheared wavefronts form an interference pattern in the region of overlap in the observation plane, as shown in Figure 10.

The fringes in the interference pattern represent phase gradients of the test wavefront. If the test wavefront has a small curvature, the interference pattern exhibits straight fringes, perpendicular to the direction of shear. The number of fringes in the interference pattern is a function of both the curvature and magnitude of shear.

In the vortex lattice generation by interference of three-plane waves, the phase difference between any two waves at the observation plane is found to vary in a linear way. Linearly varying phase difference leads to straight fringes. Hence, for a given interference pattern $I(x, y)$ involving two waves with constant amplitude distribution, we have absolute freedom on choosing the phase $\psi(x, y)$ of the first wave as long as we are able to realize the other interfering wave, which can produce the required phase difference $\Delta\psi$ (which is linear) at the interference plane. This can be verified for any two-plane waves or spherical waves:

$$\left|1+\exp(-i2\pi\mu x)\right|^2 = \left|\exp\left(\frac{ik}{2R}(x^2+y^2)\right)+\exp\left(\frac{ik}{2R}\left((x+\Delta x)^2+y^2\right)\right)\right|^2 \quad (5)$$

provided $(\Delta x)^2$ is negligible and $2\pi\mu = (k/R)\Delta x$. Here R is the radius of curvature of the beam. In this example, the first term on the left hand side is the complex amplitude distribution at the z plane for an on-axis plane wave, and the second term is for a plane wave with tilt to the z axis at an angle given by $\theta = \sin^{-1}(\mu\lambda)$ where μ is the spatial frequency and λ is the wavelength of the light. On the right hand side of (5), the first term is a spherical wave under quadratic phase approximation, and the second term is the spherical wave which is sheared in the x direction by Δx. Hence, in case of the interference of spherical waves, the linear phase difference variations $\Delta\psi$ in the x and y directions are brought about by shears in the x and y directions, respectively. The amplitude of the interfering waves is kept constant, and this provides a better contrast of fringes. It is important to note that when the beam is perfectly collimated, parallel plate will not give any fringes. Fringes are formed only when the lens is decollimated and spherical wavefronts are formed [63]. Another striking and interesting aspect observed is that while interference fringes are described by phase differences, the phase distribution of the resultant field is completely different when compared with the case of vortex generation by plane wave interference. But, a regular grid of vortex dipoles is generated in both the cases. One possible configuration of the interferometer for vortex lattice generation is given in Figure 11. The observed intensity pattern at the output of the interferometer is shown in Figure 12(a). To reveal the vortex lattice in the interference pattern, a fourth beam is superposed to obtain fork fringes at the vortex points as shown in Figure 12(b).

There is also another area of research, namely, the vortex metrology. In vortex metrology [64–67], vortices which are randomly distributed in a speckle field, are tracked for metrological applications. This is different from OVI, because in OVI the regular grid of vortices act as a reference and the movement of vortex cores upon deformation of one of the interfering beams is tracked. This method has been used for measuring small displacements and also in fluid dynamics. In the [68], a similar problem for a laser beam probing the atmosphere was solved. The obtained speckle pattern was investigated through the optical vortex localization.

The study of optical vortices in microscopy was started with Tychynsky [69–72]. He proposed to measure the phase dislocations propagating in the zero-order diffraction beam. The beam was highly magnified (up to 10000 times) and interfered with a reference beam whose phase was controlled by moving mirror (phase-shifting interferometry). The other approach was to introduce the vortex into a scanning microscope and analyze the behavior of vortex after reflection

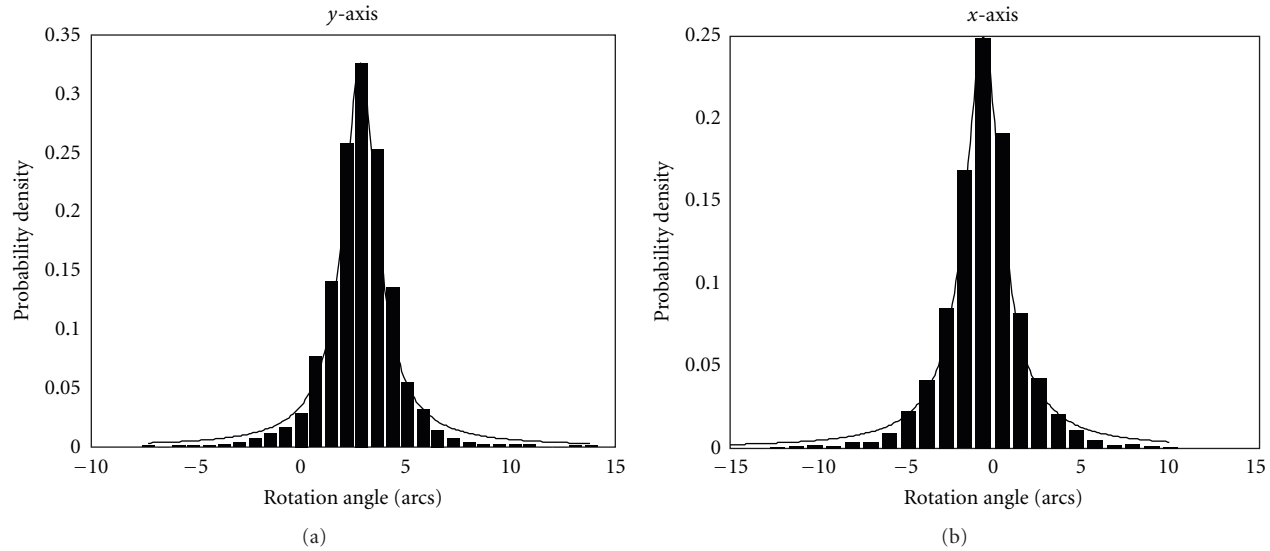

Figure 6: The angle of wave tilt (wave rotation) determined for x and y axes by analyzing the vortex triplets geometry. The expected values were 2.5 second of arc through y-axis and 0 second of arc through x-axes. In this example, around 350 vortices were observed at the image area. The statistics were made for 3500 triplets. Probability density function can be described by the Lorentz distribution (when using cells instead of triplets, we get the Gaussian distribution).

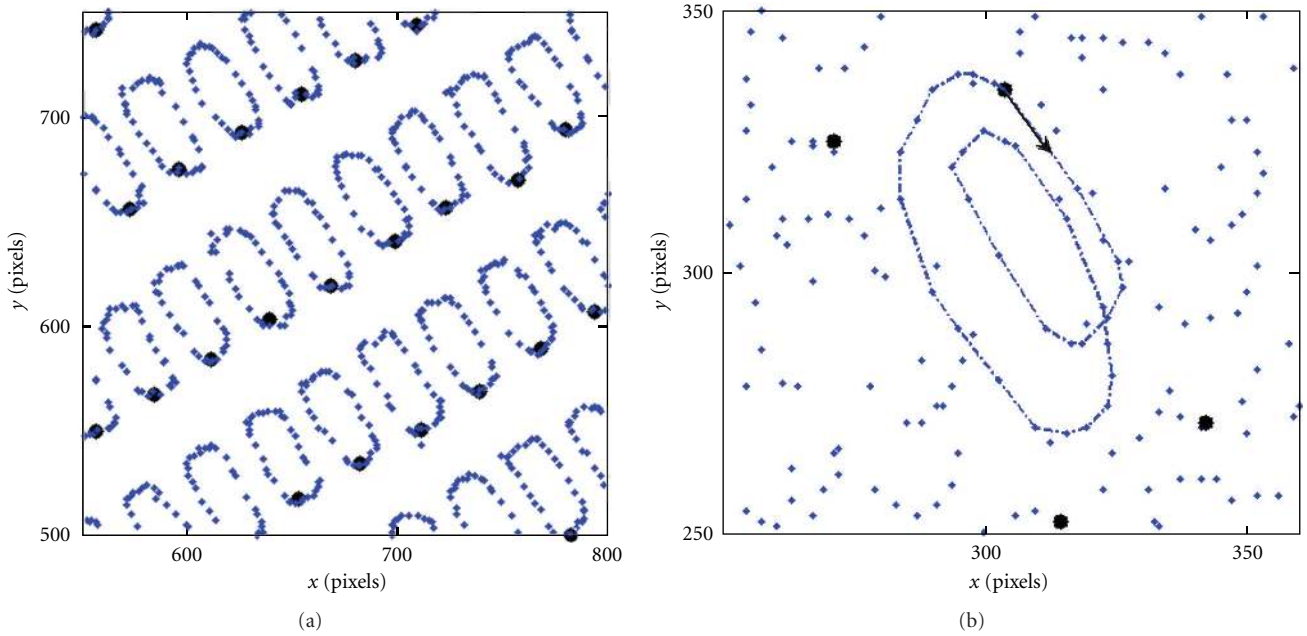

Figure 7: The trajectory of vortex points measured when a quarter wave plate is inserted between the Wollaston prism and rotated (a). The same situation applies but the quarter wave plate is wedge-like. Figure on the right shows part of the whole image.

from the sample. Since the OV may be identified by means of interference with reference beam this solution can be considered as a kind of vortex interference microscopy. This new solution has been presented in [73–79].

3. Part II

3.1. Interferometry in Polar Coordinates. The interference fringes obtained in an interferometer represent contour lines of phase difference between a test and a reference wave. By using suitable reference waves in conventional interferometers, interference fringes that are functions of polar coordinates can be obtained [80]. Such interferograms are useful since most optical elements for imaging are rotational symmetric, and it is valuable if the data is directly presented in polar coordinates. When the phase of the test wavefront varies in the radial direction, radial interferograms are advantageous, and, when the phase variation occurs

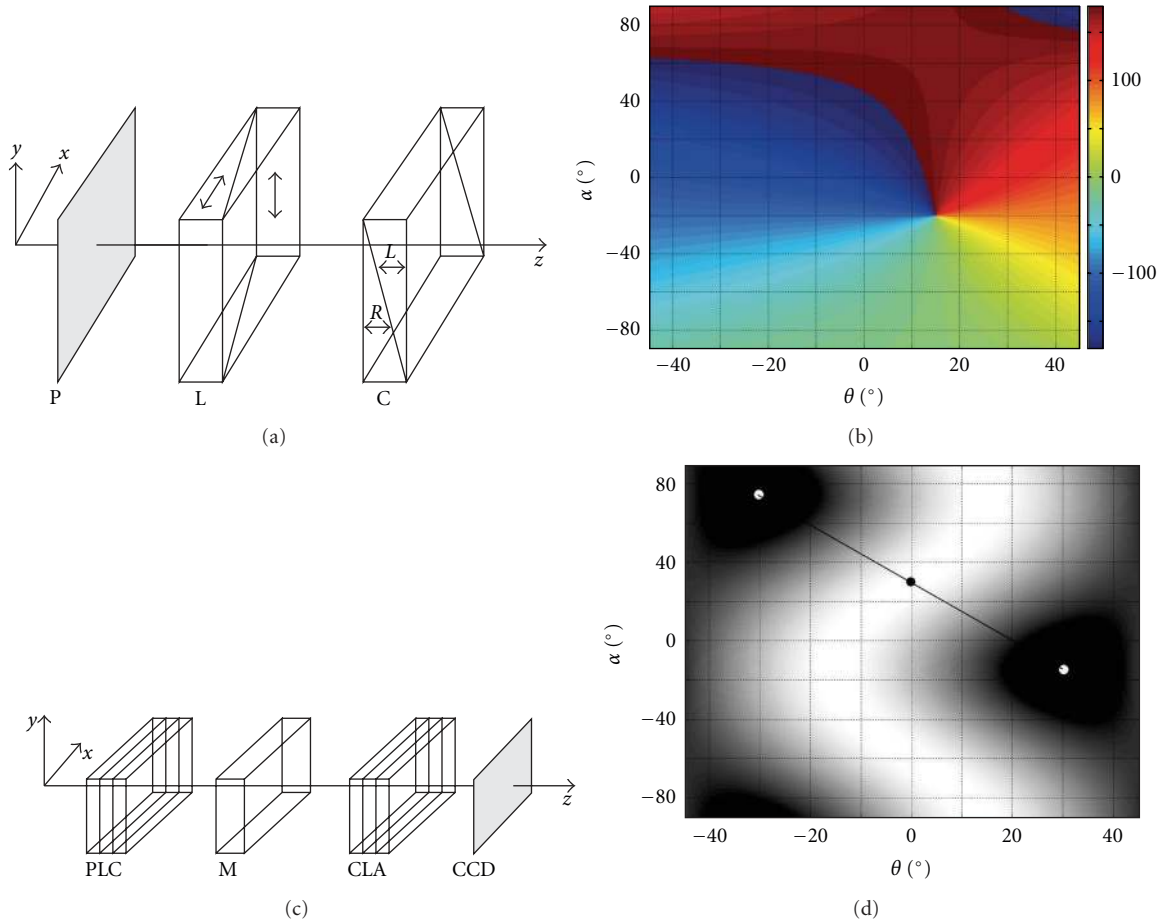

Figure 8: (a) A new polarimetric system consists of polarizer P, Wollaston prism *L*, and a circular wedge compensator *C*. This setup produces a table of all polarization states. When working in reverse direction (light incident on circular wedge compensator *C*), the optical vortex appears as shown (as a phase map) in part (b). Having the position of this vortex point, it is easy to read the polarization state of the incident light; (c) a more complex system named "spatial elliptical polariscope". Here M is a birefirngent medium under measurement. Figure (d) shows the intensity distribution with two dark points where optical vortices are seeded. Each vortex points (white points) indicate the state of the polarization of fast and slow beams, respectively. The black points show the position of maximum intensity. The distribution of these points enable determining the azimuth and ellipticity of both the beams and also the retardation between them [36].

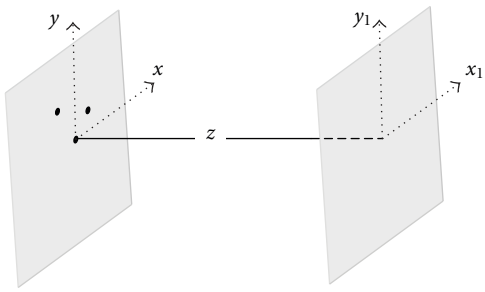

Figure 9: Schematic of the three pinholes arrangement for vortex lattice generation.

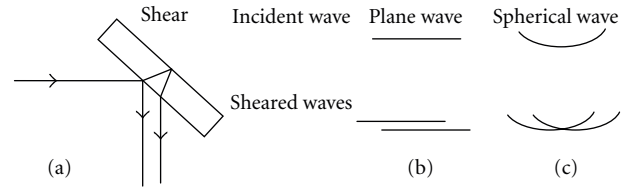

Figure 10: (a) Lateral shear interferometer in which the incident wave is split into two and sheared. (b) Schematic showing that the phase difference between sheared plane waves is constant. (c) Schematic showing the phase difference between sheared spherical waves is not constant and varies linearly in the direction of shear.

in the azimuthal direction, circular fringe interferograms are useful. It is much similar to the use of an appropriate coordinate system depending upon a variable in the problem which is also a function of some coordinate system.

Optical vortices play a crucial role in obtaining interferograms that are radial or spiral. The reference wave used in these interferometers consists of vortex-like phase variation. To obtain radial interferograms, reference wave consisting of

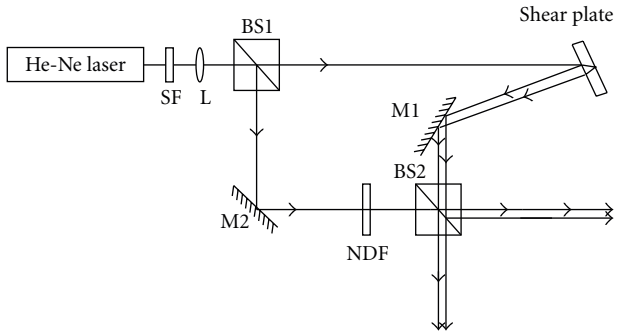

Figure 11: Experimental setup for the Mach-Zehnder interferometer configuration with shear plate inducted in one arm.

an optical vortex of multiple charge is useful. The reference wave that is used to get radial interferogram is given by $\phi_{r1} = m\theta$. To obtain spiral fringe interferograms, the reference wave phase distribution is of the form $\phi_{r2} = m\theta + Cr$, where m is the charge and C is a constant. The reference wave here is a conical wave in which vortex phase distribution is embedded. Figures 13(a) and 13(b) show the reference beams where optical vortices are used. Figures 13(c) and 13(d) are two test wavefronts in which the phase variations are azimuthal and radial respectively. In the phase distributions, dark represents zero phase, and white represents 2π phase with grey levels representing other intermediate phase values.

The phase variations of the two simulated test wavefronts are $\phi_{t1} = \pi \sin(6\theta)$ and $\phi_{t2} = \pi \cos(\alpha r^3)$, respectively.

The interferogram of Figure 14(b) is useful as the test wavefront ϕ_{t1} has an azimuthal phase variation. The spiral interferogram that would have resulted in an interference with a plane wave has a constant period in the radial direction. The fringe shift in the radial direction is a function of phase variation of the test wavefront.

The interferogram of Figure 15(a) is useful as in this case the test wavefront ϕ_{t2} has radial phase variation and the shift in the radial fringes depends on this phase variation. The advantages of polar interferograms are reported by Bryngdahl [80].

3.2. Shear Interferometry in Polar Coordinates. Shear interferometer eliminates the need for a known reference as the interference is between the test wavefront and a sheared copy of it. The fringes obtained give the phase gradient of the wavefront if the test wavefront is appropriately sheared.

While the lateral shear interferometer reveals phase gradients in Cartesian coordinates, it is essential to modify the way shear is applied for obtaining gradient in polar coordinates. The gradient of the complex amplitude u in polar coordinates is given by

$$\nabla u = \frac{\partial u}{\partial r}\hat{r} + \frac{1}{r}\frac{\partial u}{\partial \varphi}\hat{\varphi}. \tag{6}$$

Thus, to study gradients with shearing interferometers, we need to introduce wavefront displacements that are constant in both the radial and azimuthal directions. In order to realize a shearing interferometer that displays gradients in the azimuthal direction, all of the object points in one of the wavefronts need to be displaced by the same distance relative to the corresponding points in the other, along circular arcs, with the origin as center. Thus, rotation of the wavefront, with the amount of rotation dependent on the radius, is required. Points near to the origin are rotated by larger amount where as points away from the origin are rotated by less amount, but, in each case, the displacement along the circular arc is of equal length.

Bryngdahl and Lee [81] have used computer-generated gratings as shown in Figures 16 and 17 to achieve constant azimuthal and constant radial displacements to the wavefronts. These gratings have spiral and segmented spiral grating elements that are associated with optical vortices.

In the grating shown in Figure 16, the superimposed red arrows are indicating the directions of the local grating vectors at two different locations. The diffracted orders of the wavefront behind the grating will be shifted in the radial direction. This way, radial shear between the diffracted beams can be achieved.

For constant azimuthal displacement, simple rotation about the centre of the beam will not suffice as in, simple rotation, the azimuthal displacement is different at different radial locations. In the grating shown in Figure 17, the superimposed red arrows indicate the local grating vector directions. Each of these shows that the grating vector has both radial and angular components. For the points on a circle of constant radius, the rate of change of rotation of the grating vector is faster (with respect to θ) than those points on a circle of larger radius. It can be seen that the component of the grating vector in the azimuth direction between two vectors in the same segment is the same which ensures that the diffracted light from the grating acquires a constant azimuthal shear. The segmentation has been done to reduce distortion in the sheared wavefronts.

3.3. Interferograms of Various Wavefronts with Vortex Beam. Knowledge about the nature of interferograms formed by the interference of various types of wavefronts with vortex beams is useful in many situations. Fringes obtained by the interference of vortex beams are characterized by the birth of new fringes from the middle of the interferogram. In conventional interferograms, extrema are surrounded by closed fringes, and no fringe terminates or originates at the centre of the interferogram.

When the vortex-bearing wavefronts are plane and their vortex cores coincide, purely radial fringes occur as in Figure 18(a). The number of new fringes that originate is indicative of the charges present in the interfering beams. When the locations of the vortices in the interfering beams coincide, star like, fringes are obtained [82]. The number of new fringes indicates the difference between the vortex charges in the individual interfering beams (Figures 18(a) and 18(b)). Hence, a fringe-free pattern results when both interfering beams have equal number of charges with the same polarity. The interference pattern between a tilted plane wave and a vortex results in fork fringes (Figure 18(c)). Fork fringes are commonly used in the detection of vortices. If

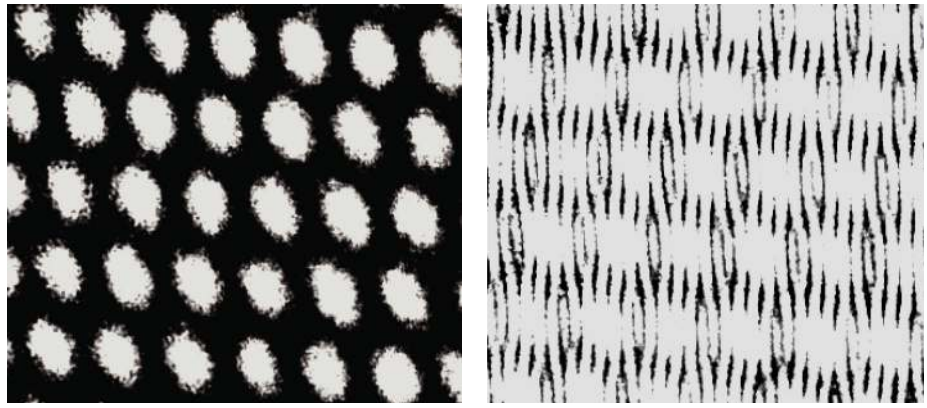

(a) (b)

Figure 12: (a). Interferogram recorded with the Mach-Zehnder interferometer configuration, (b) Formation of fork fringe pattern when fourth beam is added, indicating the presence of vortex dipole arrays.

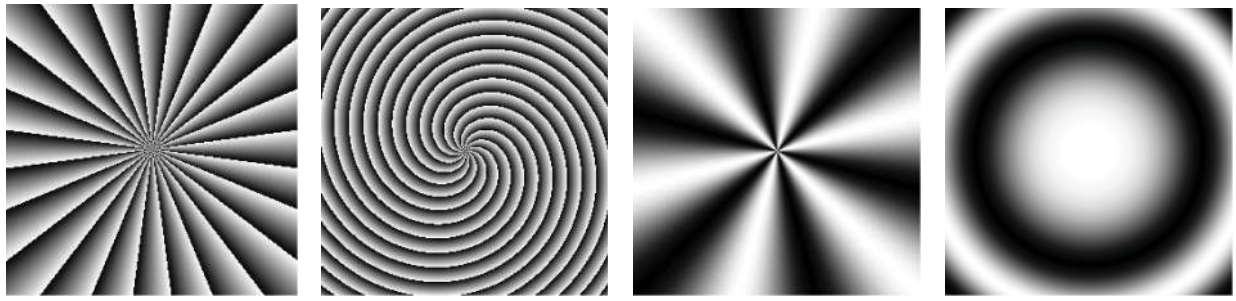

(a) (b) (c) (d)

Figure 13: The phase distributions of (a) reference wave $\phi_{r1} = m\theta$ and (b) reference wave $\phi_{r2} = m\theta + Cr$. (c) Test wave with azimuthal phase variation. (d) Test wave with radial phase variation.

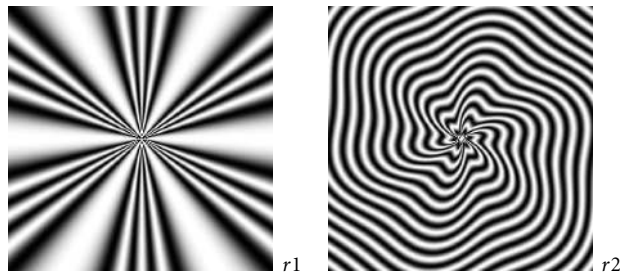

(a) (b)

Figure 14: Interferogram when the test wave ϕ_{t1} of Figure 13(c) interferes with (a) reference wave $\phi_{r1} = m\theta$ and (b) reference wave $\phi_{r2} = m\theta + Cr$.

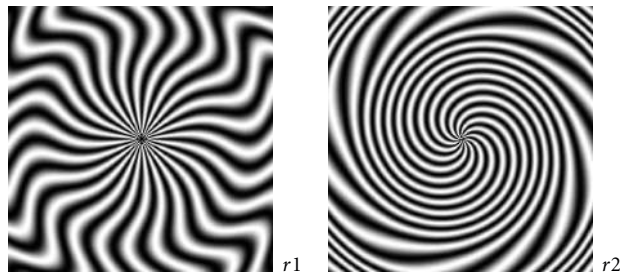

(a) (b)

Figure 15: Interferogram when the test wave ϕ_{t2} of Figure 13(d) interferes with (a) reference wave $\phi_{r1} = m\theta$ (b) reference wave $\phi_{r2} = m\theta + Cr$.

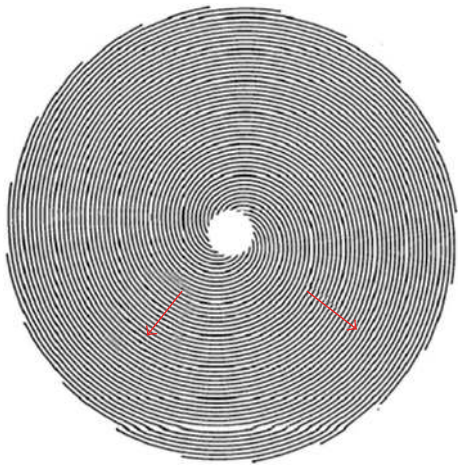

Figure 16: Grating that introduces a constant radial displacement between sheared wavefronts [81].

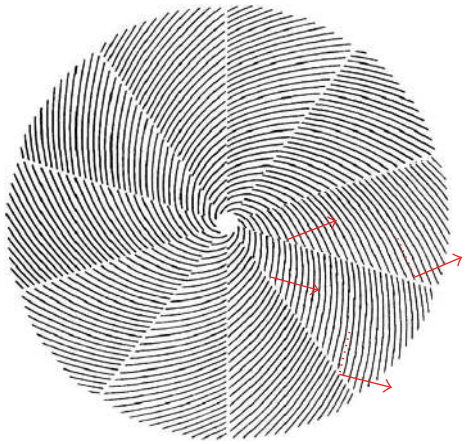

Figure 17: Segmented spiral grating that can used to introduce a constant azimuthal displacement between sheared wavefronts [81].

the interferogram consists of a fork pattern anywhere in the field of view, it is inferred that one of the interfering waves has a singularity. Diffraction phenomenon can also be used for the detection of vortices [83]. When the cores of the vortices of the interfering waves do not coincide, the total number of fringes obtained is different in the cases of beams with opposite and similar polarity. In the former case, it is exactly equal to the charge of the beam with the higher charge value (Figure 18(d)), whereas, in the latter case, it equals the sum of the charges of the two (Figure 18(e)). Interferograms shown in Figure 18(d) are due to interference of two singular beams having charges +8 and −2, respectively, where as in Figure 18(e), the interfering beams have charges +8 and +2, respectively.

The radial fringes shown in Figure 18(b) start to spiral in the anticlockwise direction when the interfering beam acquires a positive curvature (Figure 19(a)) and spiral clockwise direction (Figure 19(b)) when the interfering beam acquires a negative curvature. This phenomenon can be used to detect beam collimation. At collimation, radial fringes can be obtained [82]. Interference of spherical beam with a plane reference wave gives rise to concentric circular fringes irrespective of the sign of the curvature of the spherical wave. If the plane reference beam is replaced by a vortex beam, spiral interferograms can be obtained. This enables us to distinguish the extremum between peak and valley [84]. When the interfering wave is a conical wave, the resulting spiral interferogram will have a fringe spacing that is constant in the radial direction (Figure 19(c)). Such interferogram can be recorded to make gratings that are useful in obtaining radial shear [80]. When the extrema (in the phase map) of the spiral wavefront do not coincide with the core of the vortex during interference, fringes as shown in Figure 19(d) are obtained [85]. One of the circular fringes at the vortex point branches (forks). As a result fringes start to spiral only from this point, and we see both circular and spiral fringes in the same interferogram. Thus, we see, in Figure 19(d), two circular fringes at the center of the interferogram and spiral fringes thereafter. Such recorded interferograms can be used as holograms, which reconstruct the vortex beam when illuminated by a beam free of vortices. When sinusoidal amplitude fork grating (with charge $+m$) is illuminated by a plane wave, the different diffraction orders -1, 0, and $+1$ produce beams with topological charge $-m$, 0 and $+m$, respectively. If the fork grating (with charge $+m$) is a binary amplitude or a phase grating, beams in each of the multiple diffraction orders contain vortices of charge mp, where p is the integral diffraction order number. Recordings of the interferograms shown in Figures 19(a) and 19(b) yield spiral zone plates [86], and recording of interferogram shown in Figure 18(c) yields fork grating. These elements are commonly used for vortex generation. In the recording of Figure 19(b), if the signs of the curvature of the spherical beam and the charge of the vortex are simultaneously reversed, interferogram shown in Figure 19(e) can be obtained. Equivalently, we can say that a fork grating with its fork up can be generated either by the interference of a singular beam with a positive vortex and an off-axes beam with positive tilt or by the interference of a singular beam with a negative vortex and an off-axis beam with a negative tilt.

3.4. Vortex Interferometry with Orthogonally Polarized Light Waves. In this section, we show the synthesis of a vortex beam by a superposition of beams with a polarization singularity using an interferometer. In other words, scalar beams with a phase singularity and vector beams with a polarization singularity can be mutually converted.

3.4.1. Laguerre-Gaussian Beams. The optical beam generated in an optical resonator is a solution of the wave equation. When the scalar wave equation, commonly referred to as the Helmholtz equation, is solved, the solution is a linearly polarized optical beam with homogeneous spatial distribution across the beam cross section. Hermite-Gaussian (HG) beams are the typical paraxial solutions obtained in the orthogonal coordinate system. In the cylindrical coordinate system, Laguerre-Gaussian (LG) and Bessel-Gaussian (BG)

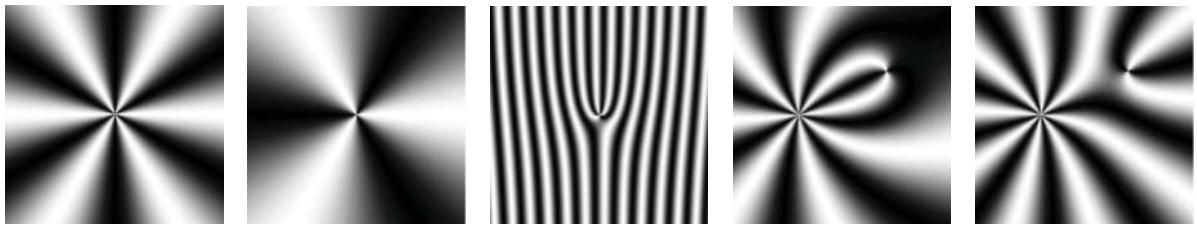

(a) (b) (c) (d) (e)

Figure 18: Fringes obtained due to interference between a vortex of charge +3 with (a) another beam with charge −3 (b) an on-axis plane wave (c) an off-axis plane wave. Interferograms obtained when both the interfering beams have off centred vortices of (d) opposite unequal charges (e) same signed unequal charges.

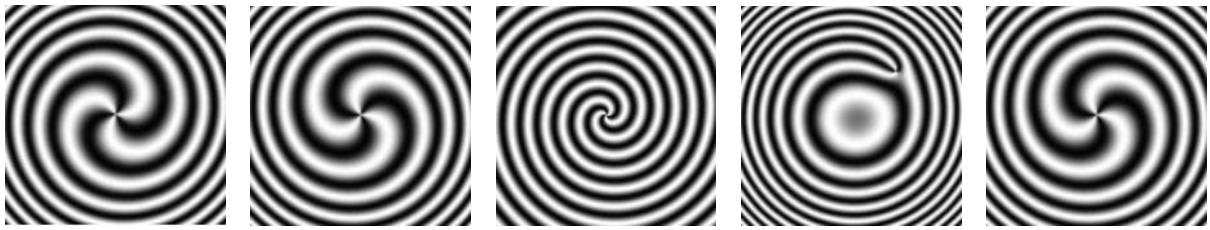

(a) (b) (c) (d) (e)

Figure 19: Fringes obtained due to interference between a vortex of charge 3 with (a) Spherical beam of positive curvature (b) spherical beam of negative curvature (c) conical beam. (d) Interference between an off centred vortex and a spherical wave (e) Interference between negatively charged vortex and a spherical beam with positive curvature.

beams are derived and are well known as vortex beams. The electric field of scalar LG beam of degree p and order m is expressed by

$$E^{(s)}_{p,m}(r,\phi,z) \propto Y_{p,m}(r,\phi,z)\exp(im\phi), \tag{7}$$

$$\begin{aligned} Y_{p,m}(r,\phi,z) = {} & \frac{\omega_0}{\omega(z)}\left[\frac{\sqrt{2}r}{\omega(z)}\right]^{|m|} L_p^{|m|}\left[\frac{2r^2}{w^2(z)}\right] \\ & \times \exp[ikz - i(2p+|m|+1)\psi(z)] \\ & \times \exp\left\{-r^2\left[\frac{1}{\omega^2(z)} - \frac{ik}{2R(z)}\right]\right\}, \end{aligned} \tag{8}$$

where r is the radius, ϕ is the azimuthal angle, z is the distance from the beam waist, ω_0 is the minimum beam radius at $z = 0$, $R = (z^2 + {z_0}^2)/z$ is the radius of curvature of the wave front, k is the wave number, $(2p + |m| + 1)\psi(z)$ is the Gouy phase shift with $\psi(z) = \arctan(z/z_0)$, and $\omega(z)$ is the Gaussian beam width defined as $\omega(z) = \omega_0\sqrt{1 + (z/z_0)^2}$ with $z_0 = k{\omega_0}^2/2$. $L_p^m(t)$ is the Laguerre polynomial of degree p and order m. The beam is assumed to propagate in the z direction. The last term of (7), $\exp(im\phi)$, indicates that the beams have a spiral phase shift with m revolutions about the axis of the optical beam. The number m is the topological charge and is indicative of the beam carrying an orbital angular momentum [21]. This equation implies that beams with $m \geq 1$ have an intensity null on the beam axis, which corresponds to a point phase singularity. The Bessel-Gaussian beams also have a spiral phase shift and, hence, a point phase singularity.

If the polarization of the optical beam is inhomogeneous, optical beams must be derived by solving the vector wave equation. The solutions of this equation are different from those of the Helmholtz equation. LG [87], BG [88], and modified BG [89] beams are the solutions in the cylindrical coordinate system. The electric field of vector LG beam of degree p and order $m \pm 1$ is expressed by

$$\begin{aligned} & \mathbf{E}^{(v)}_{p,m\pm1}(r,\phi,z) \\ & \quad \propto Y_{p,m\pm1}(r,\phi,z)\begin{Bmatrix} \mp\sin(m\phi)\boldsymbol{\rho} + \cos(m\phi)\boldsymbol{\varphi} \\ \cos(m\phi)\boldsymbol{\rho} \pm \sin(m\phi)\boldsymbol{\varphi} \end{Bmatrix}, \end{aligned} \tag{9}$$

where $\boldsymbol{\rho}$ and $\boldsymbol{\varphi}$ are the unit vectors of the electric field for the radial and azimuthal directions, respectively. Equation (9) shows that these beams do not have a spiral phase shift but a complicated distribution of polarization as shown by the last term. All beams also have an intensity null on the beam axis due to the presence of a point singularity. Note that this is not a phase singularity but a singularity of polarization. Thus, there is an inherent difference of singularities between scalar and vector LG beams.

The lowest-order mode of vector LG beams is obtained for $m = 0$. In this case, the beam carries pure azimuthal and radial polarizations for upper and lower rows of (9), respectively. The temporal electric field distributions of these two lowest order LG beams are depicted in Figure 20. An azimuthally polarized beam is shown in Figure 20(a), which is called TE_{01} mode because there is no electric field in the direction of beam propagation. The other beam shown in Figure 20(b) is a radially polarized beam, which has no

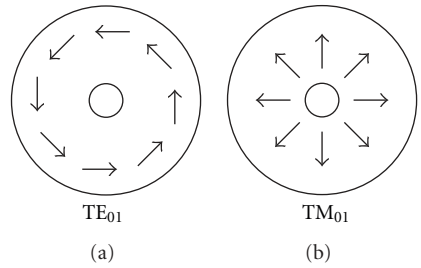

Figure 20: The lowest-order vector LG beams. (a) Azimuthally (TE_{01}) and (b) radially (TM_{01}) polarized, respectively. The arrows indicate the direction of the temporal electric field.

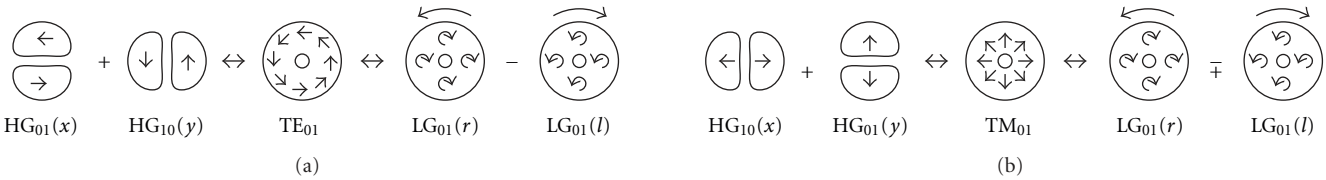

Figure 21: The conversion between scalar and vector LG beams. (a) Azimuthally and (b) radially polarized beams. x and y in the parentheses for linearly polarized HG beams indicate the polarization direction. r and l in the parentheses for circularly polarized LG beams indicate right- and left-hand polarizations, respectively. HG: Hermite-Gaussian beam, LG: Laguerre-Gaussian beam.

magnetic field in the direction of propagation (TM_{01} mode). The small circle in the center is the dark area due to the polarization singularity on the beam axis. In what follows, we will show that these beams can also be synthesized by a superposition of scalar beams with a phase singularity.

As shown in Figure 21(a), an azimuthally polarized beam can be expressed by a superposition of two linearly polarized HG beams with orthogonal polarizations, that is, HG_{01} mode with x-polarization and HG_{10} mode with y-polarization. Note that these HG beams have a line phase singularity. Similarly, a radially polarized beam can be expressed by a superposition of HG_{10} mode with x-polarization and HG_{01} mode with y-polarization as shown in Figure 21(b). Another superposition is possible as shown in the right-hand side of Figure 21. In these cases, radially and azimuthally polarized beams are superpositions of circularly polarized LG_{01} beams with inverse handedness of both spin and orbital angular momenta, that is, right- and left-hand circularly polarized LG_{01} beams superposed with beams carrying left- and right-hand orbital angular momenta, respectively. Note that there is π, phase shift between two left-handed circularly polarized LG_{01} beams, namely, subtraction and addition in Figures 21(a) and 21(b), respectively.

These transformations between scalar and vector LG beams have been experimentally demonstrated by Tidwell et al. [90] using a Mach-Zehnder interferometer and a linearly polarized Ar ion laser beam with a Gaussian intensity profile (TEM_{00} mode). Although the manipulation of polarization is not difficult, the production of higher transverse modes such as HG_{01} and LG_{01} modes needed the use of unconventional phase elements. For the HG_{01} mode, a half part of a TEM_{00} mode beam was passed through a tilted glass plate, whose angle was adjusted to obtain a π phase shift between the two semicircular parts of the beam. LG_{01} mode beams were produced by passing a TEM_{00} mode beam through a spiral phase delay plate, which had a spiral ramp made from thin-film-coated glass plate resulting in the relative phase shift of π. Although the synthesis of radially and azimuthally polarized beams has been verified, there have still been some drawbacks. The first method using two linearly polarized HG_{01} beams was sensitive to the intensity profile error of an input TEM_{00} mode beam. The second one using LG_{01} beams had a low conversion efficiency (<50%) because two circularly polarized beams were combined by a conventional polarization beam splitter for linear polarization. These problems have been solved based on the fact that a linearly polarized HG_{01} mode is a superposition of two linearly polarized LG_{01} modes carrying inverse orbital angular momenta [91]. Figure 22 shows the case for the generation of an azimuthally polarized beam shown in Figure 20(a). In Figure 22(a), a HG_{01} mode is expressed by a superposition of two LG_{01} modes with inverse orbital angular momenta and π-phase shift (subtraction). In the same manner, a HG_{10} mode is expressed by an addition of two LG_{01} modes. Since the polarizations are linear and the intensity patterns are doughnut, the drawbacks in the previous methods are improved. In addition, this method implies that vector LG_{01} beams with a polarization singularity on the beam axis can be converted from scalar LG_{01} beams with a phase singularity on the beam axis similar to the conversion shown on the right-hand side of Figure 21. Some improvements based on a similar principle have been demonstrated using a simpler phase element [92] and a Sagnac's interferometer [93].

The generation of pure radially and azimuthally polarized beams directly from a laser cavity has also been demonstrated [94] based on the same principle as shown in Figure 21(b). In this experiment, HG_{01} and HG_{10} beams are generated and combined in a laser cavity using linear

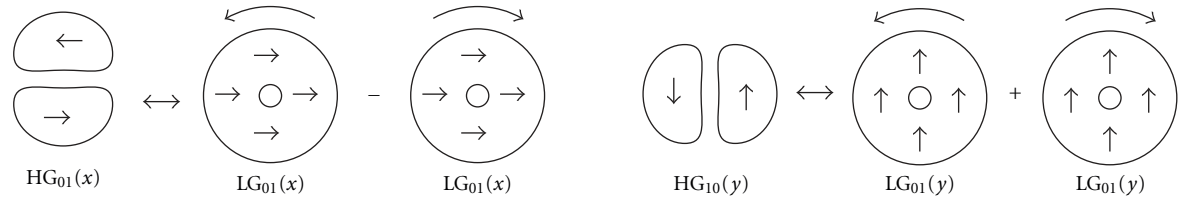

Figure 22: Conversion between linearly polarized HG and LG modes.

polarization optics and a π-phase shifter. Recent progresses on vector beams are reviewed [95].

In the following, we show that the conversion between scalar and vector LG beams mentioned above is generally concluded. The upper row of (9) can be expressed by a superposition of two LG_{01} modes with opposite spin and orbital angular momenta in the following way:

$$\begin{aligned}
&E^{(s)}_{p,\mp(m\pm1)}(\mathbf{x}+i\mathbf{y}) - E^{(s)}_{p,\pm(m\pm1)}(\mathbf{x}-i\mathbf{y}) \\
&\quad\propto Y_{p,m\pm1}\{\exp[\mp i(m\pm1)\phi](\mathbf{x}+i\mathbf{y}) \\
&\qquad\qquad - \exp[\pm i(m\pm1)\phi](\mathbf{x}-i\mathbf{y})\} \\
&\quad= Y_{p,m\pm1}\{\exp[\mp i(m\pm1)\phi]\exp(i\phi)(\boldsymbol{\rho}+i\boldsymbol{\varphi}) \\
&\qquad\qquad - \exp[\pm i(m\pm1)\phi]\exp(-i\phi)(\boldsymbol{\rho}-i\boldsymbol{\varphi})\} \\
&\quad= Y_{p,m\pm1}\{\mp[\exp(im\phi) - \exp(-im\phi)]\boldsymbol{\rho} \\
&\qquad\qquad + i[\exp(im\phi) + \exp(-im\phi)]\boldsymbol{\varphi}\} \\
&\quad= 2iY_{p,m\pm1}[\mp\sin(m\phi)\boldsymbol{\rho} + \cos(m\phi)\boldsymbol{\varphi}] \\
&\quad\propto \mathbf{E}^{(v)}_{p,m\pm1}(\text{upper row}),
\end{aligned} \tag{10}$$

where $\mathbf{x}$ and $\mathbf{y}$ are the unit vectors of the electric field for the x and y directions in the orthogonal coordinate system, respectively. In the same way, the lower row of (9) can be expressed as

$$\begin{aligned}
&E^{(s)}_{p,\mp(m\pm1)}(\mathbf{x}+i\mathbf{y}) + E^{(s)}_{p,\pm(m\pm1)}(\mathbf{x}-i\mathbf{y}) \\
&\quad\propto Y_{p,m\pm1}\{\exp[\mp i(m\pm1)\phi](\mathbf{x}+i\mathbf{y}) \\
&\qquad\qquad + \exp[\pm i(m\pm1)\phi](\mathbf{x}-i\mathbf{y})\} \\
&\quad= Y_{p,m\pm1}\{\exp[\mp i(m\pm1)\phi]\exp(i\phi)(\boldsymbol{\rho}+i\boldsymbol{\varphi}) \\
&\qquad\qquad + \exp[\pm i(m\pm1)\phi]\exp(-i\phi)(\boldsymbol{\rho}-i\boldsymbol{\varphi})\} \\
&\quad= Y_{p,m\pm1}\{[\exp(im\phi) + \exp(-im\phi)]\boldsymbol{\rho} \\
&\qquad\qquad \mp i[\exp(im\phi) - \exp(-im\phi)]\boldsymbol{\varphi}\} \\
&\quad= 2Y_{p,m\pm1}[\cos(m\phi)\boldsymbol{\rho} \pm \sin(m\phi)\boldsymbol{\varphi}] \\
&\quad\propto \mathbf{E}^{(v)}_{p,m\pm1}(\text{lower row}).
\end{aligned} \tag{11}$$

The relation, $\mathbf{x} \pm i\mathbf{y} = (\boldsymbol{\rho}\cos\phi - \boldsymbol{\varphi}\sin\phi) \pm i(\boldsymbol{\rho}\sin\phi + \boldsymbol{\varphi}\cos\phi) = \exp(\pm i\phi)(\boldsymbol{\rho} \pm i\boldsymbol{\varphi})$, played an important role in the above conversion. The expression is indicative that a spin angular momentum can be represented by an orbital angular momentum, in other words, a polarization singularity is related to a phase singularity. While (10) and (11) are the derivation of a vector LG mode from scalar LG modes, the derivation in the opposite way is also possible as shown in the following:

$$\begin{aligned}
&\mathbf{E}^{(v)}_{p,m+1}(\text{upper row}) \pm i\mathbf{E}^{(v)}_{p,m+1}(\text{lower row}) \\
&\qquad = \pm iE^{(s)}_{p,\pm(m+1)}(\mathbf{x}\mp i\mathbf{y}), \\
&\mathbf{E}^{(v)}_{p,m-1}(\text{upper row}) \pm i\mathbf{E}^{(v)}_{p,m-1}(\text{lower row}) \\
&\qquad = \pm iE^{(s)}_{p,\mp(m-1)}(\mathbf{x}\mp i\mathbf{y}).
\end{aligned} \tag{12}$$

In the above expressions, circularly polarized LG modes are derived by a superposition of two vector LG modes.

3.4.2. Bessel-Gaussian Beams. The electric fields of scalar and vector BG beams, $E^{s-\mathrm{BG}}_m(r,\phi,z)$ and $\mathbf{E}^{v-\mathrm{BG}}_m(r,\phi,z)$, respectively, are expressed by

$$E^{s-BG}_m(r,\phi,z) \propto Z(r,\phi,z)i^m J_m(u)\exp(im\phi), \tag{13}$$

$$\mathbf{E}^{v-BG}_m(r,\phi,z) \propto Z(r,\phi,z)\mathbf{T}_m(r,\phi,z), \tag{14}$$

$$\begin{aligned}
&Z(r,\phi,z) \\
&= \frac{\omega_0}{\omega(z)}\exp[ikz - i\psi(z)]\exp\left\{-r^2\left[\frac{1}{\omega^2(z)} - \frac{ik}{2R(z)}\right]\right\}, \\
&\quad\times\exp\left\{-\frac{i\beta^2 z}{2k(1+iz/z_0)}\right\},
\end{aligned} \tag{15}$$

where β is a constant, $J_m(u)$ is the Bessel function of the first kind of order m, and $u = \beta r/(1+iz/z_0)$. $\mathbf{T}_m(r,\phi,z)$ has two

families transverse electric field solutions $\mathbf{TE}_m$ and transverse magnetic field solution $\mathbf{TM}_m$ [88], expressed by

$$\begin{aligned}\mathbf{TE}_m(r,\phi,z) &= [J_{m-1}(u) - J_{m+1}(u)]\begin{bmatrix}-\sin(m\phi)\\ \cos(m\phi)\end{bmatrix}\boldsymbol{\varphi}\\ &\quad + [J_{m-1}(u) + J_{m+1}(u)]\begin{bmatrix}\cos(m\phi)\\ \sin(m\phi)\end{bmatrix}\boldsymbol{\rho},\\ \mathbf{TM}_m(r,\phi,z) &= -[J_{m-1}(u) + J_{m+1}(u)]\begin{bmatrix}\cos(m\phi)\\ \sin(m\phi)\end{bmatrix}\boldsymbol{\varphi}\\ &\quad + [J_{m-1}(u) - J_{m+1}(u)]\begin{bmatrix}-\sin(m\phi)\\ \cos(m\phi)\end{bmatrix}\boldsymbol{\rho}.\end{aligned} \tag{16}$$

Equation (13) shows that a scalar BG beam with the Bessel function of order m has a topological charge of m and a point phase singularity on the beam axis except for $m = 0$. On the other hand, vector BG beams have a point polarization singularity on the beam axis except for $m = 1$, where the order of the Bessel function is zero, and the beam has a finite intensity on the beam axis. Although the intensity distribution of vector BG beams is more complicated compared to that of a vector LG beam, the conversion between scalar and vector BG beams is also possible. For example, the equation in the upper row of $\mathbf{TE}_m$ is derived by a superposition of four scalar BG beams with circular polarization as mentioned below.

$$\begin{aligned}&\left[E_{m-1}^{s-BG} - E_{-(m+1)}^{s-BG}\right](\mathbf{x}+i\mathbf{y}) + \left[E_{-(m-1)}^{s-BG} - E_{m+1}^{s-BG}\right](\mathbf{x}-i\mathbf{y})\\ &\quad\propto Zi^{m-1}\{J_{m-1}\exp[i(m-1)\phi]\\ &\qquad\qquad + J_{m+1}\exp[-i(m+1)\phi]\}(\mathbf{x}+i\mathbf{y})\\ &\qquad + Zi^{m-1}\{J_{m-1}\exp[-i(m-1)\phi]\\ &\qquad\qquad + J_{m+1}\exp[i(m+1)\phi]\}(\mathbf{x}-i\mathbf{y})\\ &\quad= Zi^{m-1}J_{m-1}\{\exp[i(m-1)\phi](\mathbf{x}+i\mathbf{y})\\ &\qquad\qquad + \exp[-i(m-1)\phi](\mathbf{x}-i\mathbf{y})\}\\ &\qquad + Zi^{m-1}J_{m+1}\{\exp[-i(m+1)\phi](\mathbf{x}+i\mathbf{y})\\ &\qquad\qquad + \exp[i(m+1)\phi](\mathbf{x}-i\mathbf{y})\}\\ &\quad= 2Zi^{m-1}J_{m-1}[\cos(m\phi)\boldsymbol{\rho} - \sin(m\phi)\boldsymbol{\varphi}]\\ &\qquad + 2Zi^{m-1}J_{m+1}[\cos(m\phi)\boldsymbol{\rho} + \sin(m\phi)\boldsymbol{\varphi}]\\ &\quad= 2Zi^{m-1}\{(J_{m-1} - J_{m+1})[-\sin(m\phi)\boldsymbol{\varphi}]\\ &\qquad\qquad + (J_{m-1} + J_{m+1})\cos(m\phi)\boldsymbol{\rho}\}\\ &\quad\propto \mathbf{TE}_m(\text{upper row}).\end{aligned} \tag{17}$$

Here we used the relation,

$$\begin{aligned}E_{-m}^{s-\mathrm{BG}}(r,\phi,z) &\propto Z(r,\phi,z)i^{-m}J_{-m}(u)\exp(-im\phi)\\ &= Z(r,\phi,z)i^{m}J_{m}(u)\exp(-im\phi).\end{aligned} \tag{18}$$

In the similar way, other components of $\mathbf{TE}_m$ and $\mathbf{TM}_m$ are represented by

$$\begin{aligned}&\left[E_{m-1}^{s-\mathrm{BG}} + E_{-(m+1)}^{s-\mathrm{BG}}\right](\mathbf{x}+i\mathbf{y}) - \left[E_{-(m-1)}^{s-\mathrm{BG}} + E_{m+1}^{s-\mathrm{BG}}\right](\mathbf{x}-i\mathbf{y})\\ &\quad\propto \mathbf{TE}_m(\text{lower row}),\\ &-\left[E_{m-1}^{s-\mathrm{BG}} - E_{-(m+1)}^{s-\mathrm{BG}}\right](\mathbf{x}+i\mathbf{y}) + \left[E_{-(m-1)}^{s-\mathrm{BG}} - E_{m+1}^{s-\mathrm{BG}}\right](\mathbf{x}-i\mathbf{y})\\ &\quad\propto \mathbf{TM}_m(\text{upper row}),\\ &\left[E_{m-1}^{s-\mathrm{BG}} + E_{-(m+1)}^{s-\mathrm{BG}}\right](\mathbf{x}+i\mathbf{y}) + \left[E_{-(m-1)}^{s-\mathrm{BG}} + E_{m+1}^{s-\mathrm{BG}}\right](\mathbf{x}-i\mathbf{y})\\ &\quad\propto \mathbf{TM}_m(\text{lower row}).\end{aligned} \tag{19}$$

For $m = 0$, vector BG beams have pure azimuthal and radial polarizations corresponding to $\mathbf{TE}_0$ and $\mathbf{TM}_0$ components, respectively. In this case, the electric fields of both scalar and vector BG beams include $J_1(u)$ only. Experimental demonstration has been reported by a superposition of two scalar BG beams with orthogonal polarization generated by using a spatial light modulator [93].

4. Conclusion

In this paper we present a detailed analysis about the interferograms that form optical vortex lattices and also how these vortex lattices are used in the measurement process. An example of the displacement of the vortex cores in the lattice by the introduction of a wedge plate in the interferometer is illustrated. The various vortex lattice generation methods including the one based on multiple pinhole diffraction and another using a shear interferometer are presented. As far as beams with single optical vortex are concerned, the role played by a single vortex in realizing interferograms in polar coordinates and shear interferometry in polar coordinates are dealt with. Interferograms of vortex-infested beams with plane, spherical, and conical beams and their applications are discussed. Finally, scalar beams with phase singularity and vector beams with polarization singularity are presented. The conversion between scalar and vector LG beams and the conversion between linearly polarized HG and LG modes are also illustrated. Realization of radial and azimuthal polarization states by superposition of orthogonally polarized beams are also discussed.

References

[1] J. F. Nye and M. V. Berry, "Dislocations in wave trains," *Proc. Roy. Soc. Lond. A*, vol. 336, pp. 165–190, 1974.

[2] J. F. Nye, *Natural Focusing and Fine Structure of Light*, Institute of Physics Publishing, 1999.

[3] M. Vasnetsov and K. Staliunas, Eds., *Optical Vortices*, Nova Science, Huntington, NY, USA, 1999.

[4] M. S. Soskin and M. V. Vasnetsov, "Singular optics," *Progress in Optics*, vol. 42, pp. 219–276, 2001.

[5] M. R. Dennis, K. O'Holleran, and M. J. Padgett, "singular optics: optical vortices and polarization singularities," *Progress in Optics*, vol. 53, pp. 293–363, 2009.

[6] A. S. Desyatnikov, Y. S. Kivshar, and L. Torner, "Optical vortices and vortex solitons," *Progress in Optics*, vol. 47, pp. 291–391, 2005.

[7] K. G. Larkin, D. J. Bone, and M. A. Oldfield, "Natural demodulation of two-dimensional fringe patterns. I. General background of the spiral phase quadrature transform," *The Journal of the Optical Society of America A*, vol. 18, no. 8, pp. 1862–1870, 2001.

[8] K. G. Larkin, "Natural demodulation of two-dimensional fringe patterns. II. Stationary phase analysis of the spiral phase quadrature transform," *The Journal of the Optical Society of America A*, vol. 18, no. 8, pp. 1871–1881, 2001.

[9] D. C. Ghiglia and M. D. Pritt, *Two-Dimensional Phase Unwrapping Theory, Algorithms and Software*, John Wiley & Sons, New York, NY, USA, 1998.

[10] P. Senthilkumaran, F. Wyrowski, and H. Schimmel, "Vortex Stagnation problem in iterative Fourier transform algorithms," *Optics and Lasers in Engineering*, vol. 43, no. 1, pp. 43–56, 2005.

[11] G. A. Swartzlander Jr., "Peering into darkness with a vortex spatial filter," *Optics Letters*, vol. 26, no. 8, pp. 497–499, 2001.

[12] D. Mawet, P. Riaud, O. Absil, and J. Surdej, "Annular groove phase mask coronagraph," *The Astrophysical Journal*, vol. 633, no. 2 I, pp. 1191–1200, 2005.

[13] G. A. Swartzlander Jr., E. L. Ford, R. S. Abdul-Malik et al., "Astronomical demonstration of an optical vortex coronagraph," *Optics Express*, vol. 16, no. 14, pp. 10200–10207, 2008.

[14] K. T. Gahagan and G. A. Swartzlander Jr., "Optical vortex trapping of particles," *Optics Letters*, vol. 21, no. 11, pp. 827–829, 1996.

[15] D. G. Grier, "A revolution in optical manipulation," *Nature*, vol. 424, no. 6950, pp. 810–816, 2003.

[16] N. Friedman, A. Kaplan, and N. Davidson, "Dark optical traps for cold atoms," *Advances in Atomic, Molecular and Optical Physics*, vol. 48, pp. 99–151, 2002.

[17] D. Cojoc, V. Garbin, E. Ferrari, L. Businaro, F. Romanato, and E. D. Fabrizio, "Laser trapping and micro-manipulation using optical vortices," *Microelectronic Engineering*, vol. 78-79, no. 1–4, pp. 125–131, 2005.

[18] S. W. Hell and J. Wichmann, "Breaking the diffraction resolution limit by stimulated emission: stimulated-emission-depletion fluorescence microscopy," *Optics Letters*, vol. 19, no. 11, pp. 780–782, 1994.

[19] S. W. Hell, "Increasing the resolution of far-field fluorescence microscopy by point-spread-function engineering, topics," in *Fluorescence Spectroscopy; 5: Nonlinear and Two-Photon-Induced Fluorescence*, J. Lakowicz, Ed., pp. 361–426, Plenum Press, New York, NY, USA, 1997.

[20] T. A. Klar, E. Engel, and S. W. Hell, "Breaking Abbe's diffraction resolution limit in fluorescence microscopy with stimulated emission depletion beams of various shapes," *Physical Review E*, vol. 64, no. 6, part 2, Article ID 066613, 9 pages, 2001.

[21] L. Allen, S. M. Barnett, and M. J. Padgett, Eds., *Optical Angular Momentum*, Institute of Physics Publishing, 2003.

[22] L. Allen, M. J. Padgett, and M. Babiker, "IV the orbital angular momentum of light," *Progress in Optics*, vol. 39, pp. 291–372, 1999.

[23] K. W. Nicholls and J. F. Nye, "Three-beam model for studying dislocations in wave pulses," *Journal of Physics A*, vol. 20, no. 14, article 013, pp. 4673–4696, 1987.

[24] I. Freund, N. Shvartsman, and V. Freilikher, "Optical dislocation networks in highly random media," *Optics Communications*, vol. 101, no. 3-4, pp. 247–264, 1993.

[25] O. V. Angelsky, R. N. Besaha, and I. I. Mokhun, "Appearance of wave front dislocations under interference among beams with simple wave fronts," *Optica Applicata*, vol. 27, no. 4, pp. 273–278, 1997.

[26] M. V. Berry and M. R. Dennis, "Knotting and unknotting of phase singularities: helmholtz waves, paraxial waves and waves in 2 + 1 spacetime," *Journal of Physics A*, vol. 34, no. 42, pp. 8877–8888, 2001.

[27] M. V. Berry and M. R. Dennis, "Topological events on wave dislocation lines: birth and death of loops, and reconnection," *Journal of Physics A*, vol. 40, no. 1, pp. 65–74, 2007.

[28] K. O'Holleran, M. J. Padgett, and M. R. Dennis, "Topology of optical vortex lines formed by the interference of three, four, and five plane waves," *Optics Express*, vol. 14, no. 7, pp. 3039–3044, 2006.

[29] P. Kurzynowski, W. A. Woźniak, and M. Borwińska, "Regular lattices of polarization singularities: their generation and properties," *Journal of Optics*, vol. 12, no. 3, Article ID 035406, 2010.

[30] I. Bialynikcki-Birula and S. Bialynikcka-Birula, "Vortex lines in electromagnetic field," *Physical Review A*, vol. 67, Article ID 062114, 2003.

[31] I. Bialynicki-Birula, "Electromagnetic vortex lines riding atop null solutions of the Maxwell equations," *Journal of Optics A*, vol. 6, no. 5, pp. S181–S183, 2004.

[32] Y. Lin, D. Rivera, Z. Poole, and K. P. Chen, "Five-beam interference pattern controlled through phases and wave vectors for diamondlike photonic crystals," *Applied Optics*, vol. 45, no. 31, pp. 7971–7976, 2006.

[33] J. Becker, P. Rose, M. Boguslawski, and C. Denz, "Systematic approach to complex periodic vortex and helix lattices," *Optics Express*, vol. 19, no. 10, pp. 9848–9862, 2011.

[34] J. Masajada and B. Dubik, "Optical vortex generation by three plane wave interference," *Optics Communications*, vol. 198, no. 1–3, pp. 21–27, 2001.

[35] S. Vyas and P. Senthilkumaran, "Interferometric optical vortex array generator," *Applied Optics*, vol. 46, no. 15, pp. 2893–2898, 2007.

[36] W. A. Woźniak and P. Kurzynowski, "Compact spatial polariscope for light polarization state analysis," *Optics Express*, vol. 16, no. 14, pp. 10471–10479, 2008.

[37] J. Masajada, *Optical Vortices and Their Application to Interferometry*, Oficyna Wydawnicza Politechniki Wrocławskiej, Wrocław, Poland, 2004.

[38] J. Masajada, "The interferometry based on regular lattice of optical vortices," *Optica Applicata*, vol. 37, no. 1-2, pp. 167–185, 2007.

[39] J. Masajada, A. Popiołek-Masajada, and D. M. Wieliczka, "The interferometric system using optical vortices as phase markers," *Optics Communications*, vol. 207, no. 1–6, pp. 85–93, 2002.

[40] J. Masajada, "Small-angle rotations measurement using optical vortex interferometer," *Optics Communications*, vol. 239, no. 4-6, pp. 373–381, 2004.

[41] A. Popiołek-Masajada, M. Borwińska, and W. Frączek, "Testing a new method for small-angle rotation measurements with the optical vortex interferometer," *Measurement Science and Technology*, vol. 17, no. 4, pp. 653–658, 2006.

[42] M. Borwińska, A. Popiołek-Masajada, and B. Dubik, "Reconstruction of a plane wave's tilt and orientation using an optical vortex interferometer," *Optical Engineering*, vol. 46, no. 7, Article ID 073604, 2007.

[43] E. Frączek and J. Mroczka, "An accuracy analysis of small angle measurement using the Optical Vortex Interferometer," *Metrology and Measurement Systems*, vol. 16, no. 2, pp. 249–258, 2009.

[44] P. Kurzynowski, W. A. Woźniak, and E. Frączek, "Optical vortices generation using the Wollaston prism," *Applied Optics*, vol. 45, no. 30, pp. 7898–7903, 2006.

[45] A. Popiołek-Masajada, P. Kurzynowski, W. A. Wozniak, and M. Borwińska, "Measurements of the small wave tilt using the optical vortex interferometer with the Wollaston compensator," *Applied Optics*, vol. 46, no. 33, pp. 8039–8044, 2007.

[46] P. Kurzynowski and M. Borwińska, "Generation of vortex-type markers in a one-wave setup," *Applied Optics*, vol. 46, no. 5, pp. 676–679, 2007.

[47] M. Borwińska, A. Popiołek-Masajada, and P. Kurzynowski, "Measurements of birefringent media properties using optical vortex birefringence compensator," *Applied Optics*, vol. 46, no. 25, pp. 6419–6426, 2007.

[48] W. A. Woźniak and M. Banach, "Measurements of linearly birefringent media parameters using the optical vortex interferometer with the Wollaston compensator," *Journal of Optics A*, vol. 11, no. 9, Article ID 094024, 2009.

[49] W. Frączek and J. Mroczka, "Optical vortices as phase markers to wave-front deformation measurement," *Metrology and Measurement Systems*, vol. 15, no. 4, pp. 433–440, 2008.

[50] C. V. Felde, P. V. Polyanski, and H. V. Bogatyryova, "Comparative analysis of techniques for diagnostics of phase singularities," *Ukrainian Journal of Physical Optics*, vol. 9, no. 2, pp. 82–90, 2008.

[51] I. Mokhun and Y. Galushko, "Detection of vortex sign for scalar speckle fields," *Ukrainian Journal of Physical Optics*, vol. 9, no. 4, pp. 246–255, 2008.

[52] V. G. Denisenko, A. Minovich, A. S. Desyatnikov, W. Krolikowski, M. S. Soskin, and Y. S. Kivshar, "Mapping phases of singular scalar light fields," *Optics Letters*, vol. 33, no. 1, pp. 89–91, 2008.

[53] L. E. E. De Araujo and M. E. Anderson, "Measuring vortex charge with a triangular aperture," *Optics Letters*, vol. 36, no. 6, pp. 787–789, 2011.

[54] E. Frączek, W. Frączek, and J. Masajada, "The new method of topological charge determination of optical vortices in the interference field of the optical vortex interferometer," *Optik*, vol. 117, no. 9, pp. 423–425, 2006.

[55] E. Frączek, W. Frączek, and J. Mroczka, "The Experimental method for topological charge determination of optical vortices in a regular net," *Optical Engineering*, vol. 44, no. 2, Article ID 025601, 2005.

[56] P. Kurzynowski, M. Borwinska, and J. Masajada, "Optical vortex sign determination using self-interference methods," *Optica Applicata*, vol. 40, no. 1, pp. 165–175, 2010.

[57] J. Masajada, A. Popiołek, E. Frączek, and W. Frączek, "Vortex points localization problem in optical vortices interferometry," *Optics Communications*, vol. 234, no. 1–6, pp. 23–28, 2004.

[58] G. Budzyń, E. Frączek, W. Frączek, and J. Mroczka, "Influence of a laser beam's frequency stability on dislocation of vortex points in an optical vortex interferometer," *Applied Optics*, vol. 45, no. 17, pp. 3982–3984, 2006.

[59] A. Popiołek-Masajada and W. Frączek, "Evaluation of phase shifting method for vortex localization in optical vortex interferometry," *Journal of Optics & Laser Technology*, vol. 43, pp. 1219–1224, 2011.

[60] J. Masajada, A. Popiołek-Masajada, and M. Leniec, "Creation of vortex lattices by a wavefront division," *Optics Express*, vol. 15, no. 8, pp. 5196–5207, 2007.

[61] G. Ruben and D. M. Paganin, "Phase vortices from a Young's three-pinhole interferometer," *Physical Review E*, vol. 75, no. 2, Article ID 066613, 2007.

[62] D. P. Ghai, S. Vyas, P. Senthilkumaran, and R. S. Sirohi, "Vortex lattice generation using interferometric techniques based on lateral shearing," *Optics Communications*, vol. 282, no. 14, pp. 2692–2698, 2009.

[63] S. Vyas and P. Senthilkumaran, "Vortex array generation by interference of spherical waves," *Applied Optics*, vol. 46, no. 32, pp. 7862–7867, 2007.

[64] W. Wang, S. G. Hanson, Y. Miyamoto, and M. Takeda, "Experimental investigation of local properties and statistics of optical vortices in random wave fields," *Physical Review Letters*, vol. 94, no. 10, Article ID 103902, 2005.

[65] W. Wang, T. Yokozeki, R. Ishijima, M. Takeda, and S. G. Hanson, "Optical vortex metrology based on the core struc tures of phase singularities in Laguerre-Gauss transform of a speckle pattern," *Optics Express*, vol. 14, no. 22, pp. 10195–10206, 2006.

[66] W. Wang, N. Ishii, S. G. Hanson, Y. Miyamoto, and M. Takeda, "Phase singularities in analytic signal of white-light speckle pattern with application to micro-displacement measurement," *Optics Communications*, vol. 248, no. 1–3, pp. 59–68, 2005.

[67] W. Wang, T. Yokozeki, R. Ishijima et al., "Optical vortex metrology for nanometric speckle displacement measurement," *Optics Express*, vol. 14, no. 1, pp. 120–127, 2006.

[68] V. P. Aksenov and O. V. Tikhomirova, "Theory of singular-phase reconstruction for an optical speckle field in the turbulent atmosphere," *The Journal of the Optical Society of America A*, vol. 19, no. 2, pp. 345–355, 2002.

[69] V. P. Tychinsky, I. N. Masalov, V. L. Pankov, and D. V. Ublinsky, "Computerized phase microscope for investigation of submicron structures," *Optics Communications*, vol. 74, no. 1-2, pp. 37–40, 1989.

[70] V. P. Tychinsky, "On superresolution of phase objects," *Optics Communications*, vol. 74, no. 1-2, pp. 41–45, 1989.

[71] V. P. Tychinsky and C. H. F. Velzel, "Super-resolution in microscopy," in *Current Trends in Optics*, chapter 18, Academic Press, New York, NY, USA, 1994.

[72] C. Velzel and J. Masajada, "Superresolution phase image microscope," *Optica Applicata*, vol. 29, no. 3, pp. 293–300, 1999.

[73] B. Spektor, A. Normatov, and J. Shamir, "Experimental validation of 20nm sensitivity of Singular Beam Microscopy," in *Optical Measurement Systems for Industrial Inspection*, vol. 6616 of *Proceedings of SPIE*, Munich, Germany, June 2007.

[74] B. Spektor, A. Normatov, and J. Shamir, "Singular beam microscopy," *Applied Optics*, vol. 47, no. 4, pp. A78–A87, 2008.

[75] B. Spector, A. Normatov, and J. Shamir, "Singular beam scanning microscopy: preliminary experimental results," *Optical Engineering*, vol. 49, no. 4, Article ID 048001, 2010.

[76] J. Masajada, M. Leniec, E. Jankowska, H. Thienpont, H. Ottevaere, and V. Gomez, "Deep microstructure topography characterization with optical vortex interferometer," *Optics Express*, vol. 16, no. 23, pp. 19179–19191, 2008.

[77] J. Masajada, M. Leniec, S. Bczyńskidro, H. Thienpont, and B. Kress, "Micro-step localization using double charge optical vortex interferometer," *Optics Express*, vol. 17, no. 18, pp. 16144–16159, 2009.

[78] J. Masajada, M. Leniec, and I. Augustyniak, "Optical vortex scanning inside Gaussian beam," *Journal of Optics*, vol. 13, Article ID 035714, 2011.
[79] E. Frączek and G. Budzyn, "An analysis of an optical vortices interferometer with focused beam," *Optica Applicata*, vol. 39, no. 1, pp. 91–99, 2009.
[80] O. Bryngdahl, "Radial and Circular fringe interferograms," *The Journal of the Optical Society of America A*, vol. 63, pp. 1098–1104, 1973.
[81] O. Bryngdahl and W. H. Lee, "Shearing interferometry in polar coordinates," *The Journal of the Optical Society of America A*, vol. 64, no. 12, pp. 1606–1615, 1974.
[82] P. Senthilkumaran, "Optical phase singularities in detection of laser beam collimation," *Applied Optics*, vol. 42, no. 31, pp. 6314–6320, 2003.
[83] D. P. Ghai, P. Senthilkumaran, and R. S. Sirohi, "Single-slit diffraction of an optical beam with phase singularity," *Optics and Lasers in Engineering*, vol. 47, no. 1, pp. 123–126, 2009.
[84] S. Fürhapter, A. Jesacher, S. Bernet, and M. Ritsch-Marte, "Spiral interferometry," *Optics Letters*, vol. 30, no. 15, pp. 1953–1955, 2005.
[85] F. S. Roux, "Diffractive lens with a null in the center of its focal point," *Applied Optics*, vol. 32, no. 22, pp. 4191–4192, 1993.
[86] N. R. Heckenberg, R. McDuff, C. P. Smith, and A. G. White, "Generation of optical phase singularities by computer generated hologram," *Optics Letters*, vol. 17, pp. 221–223, 1992.
[87] A. A. Tovar, "Production and propagation of cylindrically polarized Laguerre-Gaussian laser beams," *The Journal of the Optical Society of America A*, vol. 15, no. 10, pp. 2705–2711, 1998.
[88] D. G. Hall, "Vector-beam solutions of Maxwell's wave equation," *Optics Letters*, vol. 21, no. 1, pp. 9–11, 1996.
[89] C. F. Li, "Integral transformation solution of free-space cylindrical vector beams and prediction of modified Bessel-Gaussian vector beams," *Optics Letters*, vol. 32, no. 24, pp. 3543–3545, 2007.
[90] W. C. Tidwell, D. H. Ford, and W. D. Kimura, "Generating radially polarized beams interferometrically," *Applied Optics*, vol. 29, pp. 2234–2239, 1990.
[91] S. C. Tidwell, G. H. Kim, and W. D. Kimura, "Efficient radially polarized laser beam generation with a double interferometer," *Applied Optics*, vol. 32, no. 27, pp. 5222–5229, 1993.
[92] N. Passilly, R. de Saint Denis, K. Aït-Ameur, F. Treussart, R. Hierle, and J. F. Roch, "Simple interferometric technique for generation of a radially polarized light beam," *The Journal of the Optical Society of America A*, vol. 22, no. 5, pp. 984–991, 2005.
[93] P. H. Jones, M. Rashid, M. Makita, and O. M. Maragò, "Sagnac interferometer method for synthesis of fractional polarization vortices," *Optics Letters*, vol. 34, no. 17, pp. 2560–2562, 2009.
[94] R. Oron, S. Blit, N. Davidson, A. A. Friesem, Z. Bomzon, and E. Hasman, "The formation of laser beams with pure azimuthal or radial polarization," *Applied Physics Letters*, vol. 77, no. 21, pp. 3322–3324, 2000.
[95] Q. Zhan, "Cylindrical vector beams: from mathematical concepts to applications," *Advances in Optics and Photonics*, vol. 1, no. 1, pp. 1–57, 2009.